

# Electron Microscopy Observation of TiO<sub>2</sub> Nanocrystal Evolution in High-Temperature Atomic Layer Deposition

Jian Shi,<sup>†,⊥</sup> Zhaodong Li,<sup>†</sup> Alexander Kvit,<sup>†,‡</sup> Sergiy Krylyuk,<sup>§,||</sup> Albert V. Davydov,<sup>§</sup> and Xudong Wang<sup>\*,†</sup>

<sup>†</sup>Department of Materials Science and Engineering and <sup>‡</sup>Materials Science Center, University of Wisconsin-Madison, Madison, Wisconsin 53706, United States

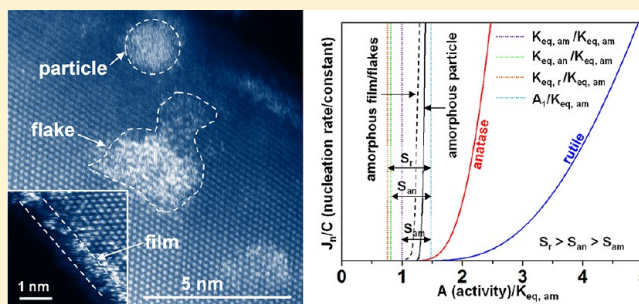
<sup>§</sup>Material Measurement Laboratory, National Institute of Standards and Technology, Gaithersburg, Maryland 20899, United States

<sup>||</sup>Institute for Research in Electronics and Applied Physics, University of Maryland, College Park, Maryland 20742, United States

## S Supporting Information

**ABSTRACT:** Understanding the evolution of amorphous and crystalline phases during atomic layer deposition (ALD) is essential for creating high quality dielectrics, multifunctional films/coatings, and predictable surface functionalization. Through comprehensive atomistic electron microscopy study of ALD TiO<sub>2</sub> nanostructures at designed growth cycles, we revealed the transformation process and sequence of atom arrangement during TiO<sub>2</sub> ALD growth. Evolution of TiO<sub>2</sub> nanostructures in ALD was found following a path from amorphous layers to amorphous particles to metastable crystallites and ultimately to stable crystalline forms. Such a phase evolution is a manifestation of the Ostwald–Lussac Law, which governs the advent sequence and amount ratio of different phases in high-temperature TiO<sub>2</sub> ALD nanostructures. The amorphous–crystalline mixture also enables a unique anisotropic crystal growth behavior at high temperature forming TiO<sub>2</sub> nanorods via the principle of vapor-phase oriented attachment.

**KEYWORDS:** TiO<sub>2</sub>, atomic layer deposition, Ostwald–Lussac law, oriented attachment



Atomic layer deposition (ALD) is a unique thin film growth technique based on sequential self-limiting surface reactions.<sup>1</sup> It offers high quality, pinhole-free, and conformal thin films with precise thickness control down to subnanometers.<sup>2</sup> During the past decades, it has demonstrated significant advancements in growing gate dielectrics in complementary metal oxide semiconductor (CMOS) devices, insulating layers in memory devices, optical coating in photonic devices, and surface modification/functionalization for catalysts.<sup>3–7</sup> Many research efforts have been devoted to explore the roughness control, surface chemical properties, and conformal coating features of ALD films, which are either amorphous or crystalline.<sup>2,8,9</sup> Contemporary research on ALD extends to exploring continuous and rapid film growth at ambient pressure and conformally depositing quantum dots, nanowires (NWs), or epitaxial films.<sup>10–19</sup> Such novel advances would make ALD a powerful and versatile nanomanufacturing tool beyond a thin film coating technique. Nevertheless, current understanding of ALD growth is mainly based on surface chemistry, that is, molecular level chemical reactions.<sup>8</sup> Although this general understanding can be adequately applied to amorphous thin film deposition at low temperature, it often meets obstacles when interpreting surface roughness, morphology, crystallinity, and physical properties.<sup>15,16</sup> Therefore, obtaining atomic-level understanding of the phase evolution in ALD is critical for achieving morphology, crystal structure,

and property control, as well as deposition manipulation and scaling.

Recently, our research revealed that by raising the deposition temperature to 600 °C, growth kinetics of TiO<sub>2</sub> ALD was modified and yielded anisotropic one-dimensional (1D) crystal growth instead of forming 2D polycrystalline films (this process was also named surface reaction-limited pulsed chemical vapor deposition, or SPCVD).<sup>14</sup> As a result, nanorod (NR) arrays were uniformly deposited inside highly confined submicrometer-sized spaces, such as inside anodized alumina oxide (AAO) nanochannels and among dense and deep Si NW forests, offering a novel hierarchical NW architecture with enhanced electrical and electrochemical properties.<sup>14,15</sup> This unique growth behavior does not follow the conventional growth models of polycrystalline or epitaxial oxides via ALD. It thus provides a valuable platform for studying and comparing phase evolution during ALD process. In this report, we present a comprehensive atomistic study of crystal nucleation and growth behaviors of TiO<sub>2</sub> nanostructures grown by ALD. By applying aberration-corrected scanning transmission electron microscopy (STEM) and TEM characterization, we revealed the transformation process and sequence of atom arrangement during high-temperature TiO<sub>2</sub> ALD growth, where the

Received: September 24, 2013

Published: October 4, 2013

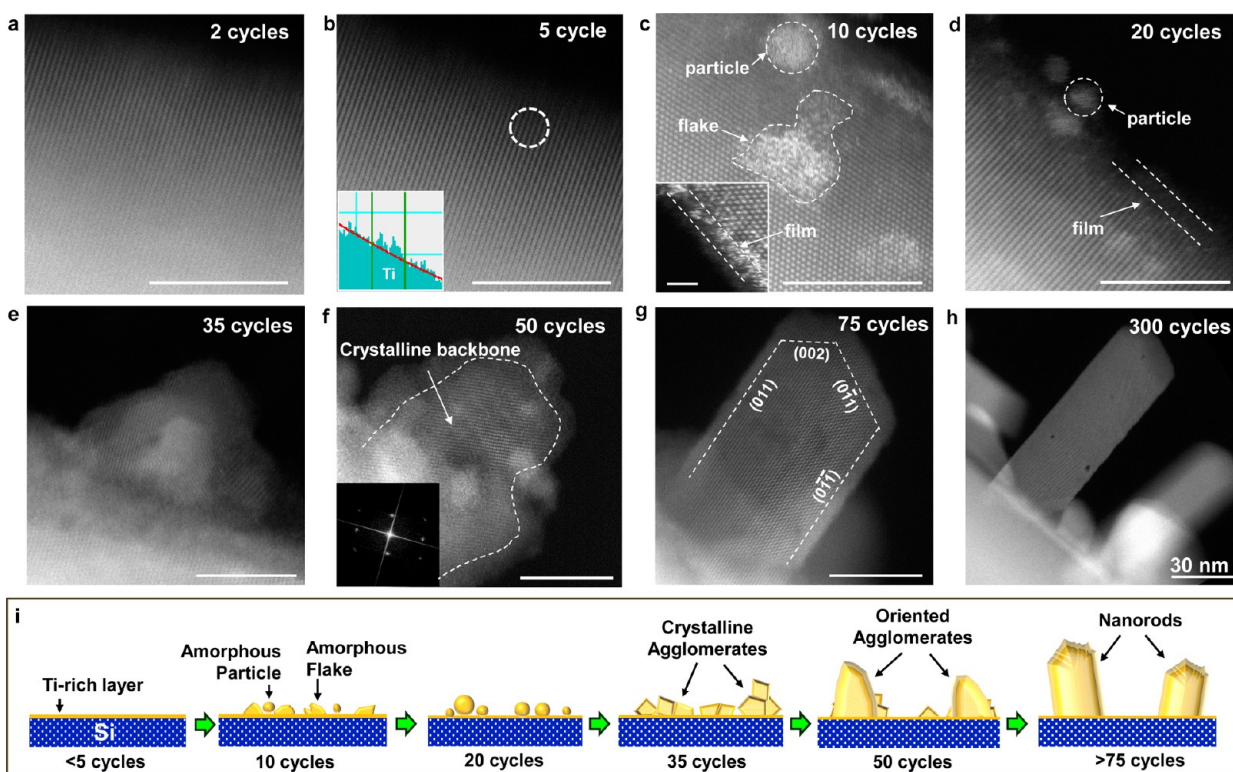


**Figure 1.** Evolution of  $\text{TiO}_2$  NRs at different ALD cycles at  $600^\circ\text{C}$  revealed by HR HAADF STEM. (a) Two cycle and (b), 5 cycle growth did not show noticeable  $\text{TiO}_x$  morphology on a single crystalline Si NW, while EELS analysis (inset of b) on 5 cycle sample detected the existence of Ti on the Si NW edge. (c) Ten cycle growth:  $\text{TiO}_x$  nanoparticles and flakes were observed on the Si NW surfaces. Inset shows the amorphous ultrathin  $\text{TiO}_x$  layer coated on NW substrate (scale bar is 1 nm). (d) Twenty cycle growth:  $\text{TiO}_x$  flakes disappeared while particles and films still existed. (e) Thirty-five cycle growth: majority of  $\text{TiO}_x$  morphology was found to be the agglomeration of amorphous layer-coated  $\text{TiO}_2$  crystallites. (f) Fifty cycle growth:  $\text{TiO}_2$  NR embryo was formed by the self-organization and alignment of individual  $\text{TiO}_2$  crystallites. Inset is the corresponding FFT pattern converted from lattice image. (g) Seventy-five cycle growth: early stage  $\text{TiO}_2$  NR was evolved with well-defined side walls and canonical growth front. (h) Three hundred cycle growth: ultimate  $\text{TiO}_2$  NR morphology was formed with two anatase (011) and two (100) as sides facets and one (0 $\bar{1}$ 1) and one (002) as growth front facets. (i) Schematic illustration of the entire evolution process of  $\text{TiO}_2$  NRs. Scale bars are 5 nm unless otherwise noted.

Ostwald–Lussac law<sup>20–22</sup> was found to be the governing rule of phase evolution. This discovery provides a new understanding of morphology and crystal evolution during ALD of crystalline nanostructures. At high temperature, the amorphous–crystalline ALD mixture can enable a unique anisotropic crystal growth behavior forming  $\text{TiO}_2$  nanorods via the principle of vapor-phase oriented attachment.

Crystal evolution was first investigated from  $\text{TiO}_2$  nanostructures deposited at  $600^\circ\text{C}$  (the conditions favoring NR formation). Detailed experimental information can be found in the Supporting Information. In order to obtain sharp interface and high-quality STEM images, single-crystalline ZnO and Si NWs were used as supporting surfaces. Figure 1 shows a series of high-resolution high-angle annular dark-field STEM (HR HAADF STEM) images taken at the interfaces between  $\text{TiO}_2$  and supporting Si NWs, where different growth stages are indexed by the ALD growth cycles. Corresponding low-magnification STEM images can be found in Supporting Information, Figure S1. At the beginning of growth (1–5 cycles), there are no noticeable  $\text{TiO}_2$  morphologies such as films or islands (Figure 1a,b); while electron energy loss spectroscopy (EELS) analysis reveals the existence of Ti elements from the Si NW edge. This is known as the initiation stage, where the deposition is controlled by reaction between precursor molecules and surface active bonds and exhibits the lowest growth rate.<sup>8</sup> At 10 cycles, three typical morphologies

emerged as shown in Figure 1c: cloudy and loosen amorphous flakes with diameters ranging from 1 to 2 nm; ultrathin amorphous film covering the surface of Si NW with a thickness of several angstroms (inset of Figure 1c); and sparsely distributed fuzzy amorphous particles with a diameter of  $\sim 1$  nm. When growth proceeds to 20 cycles, amorphous particles and ultrathin films became the dominating morphologies (Figure 1d). The density of amorphous particles at the 20-cycle stage largely increased compared to the 10-cycle samples, while similar diameters remained. In addition, no cloudy flakes were observed at this stage suggesting that the flakes are unstable transient morphology. After 35 cycles of growth, the NW surfaces were covered with larger nanoparticles (5–10 nm), which were agglomeration of small crystallites shelled by thin amorphous layers (Figure 1e and Supporting Information Figure S2). The amorphous layer surrounding the crystalline agglomeration is believed to be a fingerprint of ALD prior to phase transformation. As the growth proceeded to 50 cycles, the integrated nanoparticle assemblage became larger and its elongated shape appeared like embryos of NRs ( $\sim 10$  nm wide and  $\sim 20$  nm long, Figure 1f). Both HR HAADF STEM image and its fast Fourier transform (FFT) (right inset of Figure 1f) show that most small crystallites in the nanoparticle assemblage had the same orientation. A thin amorphous layer was also observed in the outmost region of the bulk embryos. At 75 cycles, high-density miniature NR-like single crystals of  $\sim 20$  nm

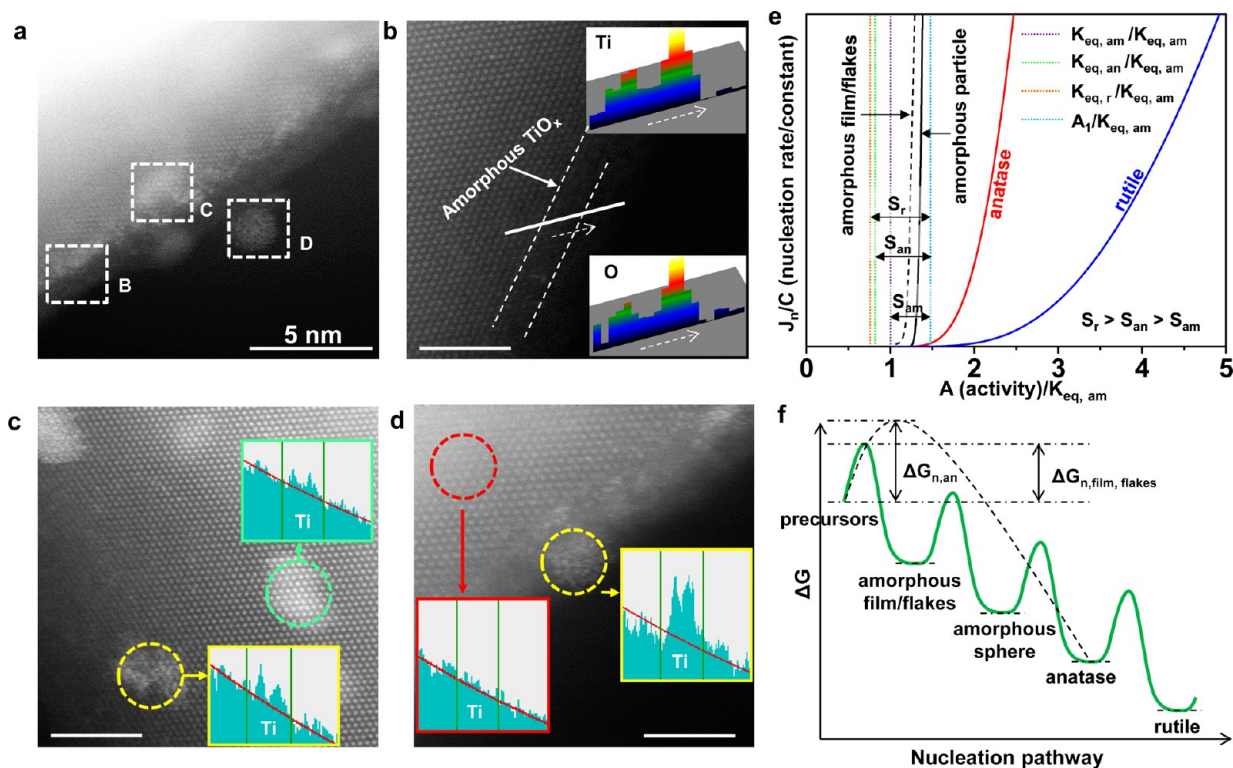


**Figure 2.** Direct observation of Ostwald–Lussac Law at 600 °C ALD growth. (a) Three typical TiO<sub>2</sub> morphologies were observed to coexist from 10-cycle ALD sample. (b) An ultrathin amorphous TiO<sub>x</sub> layer with subnanometer thickness on Si NW after 10 cycles ALD growth. Insets show the Ti and O EELS profiles (lighter color indicates stronger signals) along the indexed direction on the NW edge. (c) The flake morphology sparsely distributed on Si NW surface. Insets are EELS spectra showing the flakes have concentrated Ti. (d) The particle morphology (yellow circle) have much stronger Ti signal than flakes, while no sensible Ti signal was found from the bare NW surface. (e) Nucleation rate of different phases of TiO<sub>2</sub> versus the precursor's activity product.  $K_{eq}$  represents the equilibrium products, natural logarithms of  $S$  are defined as the supersaturations under the fixed activity  $A_1$  ( $\ln S = A_1/K_{eq}$ ). Subscripts am, an, and r stand for amorphous, anatase, and rutile phases of TiO<sub>2</sub>, respectively. (f) Schematic energy landscape of a series of TiO<sub>2</sub> phases illustrating the nucleation pathway. At certain degree of supersaturation, crystal growth tends to proceed along its adjacent crystal phases step by step toward anatase phase because the nucleation barrier of anatase TiO<sub>2</sub> ( $\Delta G_{n,an}$ ) is higher than its adjacent phases ( $\Delta G_{n, film/flake}$ ). Scale bars are 2 nm unless otherwise noted.

wide and ~40 nm long started to form (Figure 1g). Eventually, typical high-aspect ratio TiO<sub>2</sub> NRs (width, ~40 nm; length, ~200 nm) were received after longer growth cycles (Figure 1h and Supporting Information Figures S3 and S4). The entire NR evolution process is schematically shown in Figure 1i.

HR HAADF STEM observation suggests that the formation of TiO<sub>2</sub> NRs at 600 °C consists of two processes: evolution of crystallites from amorphous nanoparticles via phase transformation; and self-organization of the crystallites into polycrystalline nanoparticles assemblage. These two processes were confirmed by high-resolution transmission electron microscopy (HRTEM) (Supporting Information Figure S5), where the amorphous layer wrapping around the emerging crystallites can be clearly observed. To further confirm this self-organization process, a 25-cycle ALD amorphous TiO<sub>x</sub> film grown on silicon nitride membrane was illuminated under electron-beam in the TEM chamber (the beam current and duration conditions were optimized to reduce sample damage), while its crystal structure evolution was continuously monitored. In situ HRTEM imaging shows that the emerging crystallites first formed a chain with aligned orientations and then grew outward by attaching more crystallites (Supporting Information Figure S6). This self-organization process, known as oriented attachment growth, was originally discovered in hydrothermal growth of TiO<sub>2</sub> NWs and later was found to be a generic solution-based growth mechanism in a variety of

crystals.<sup>23,24</sup> To our best knowledge, this is the first observation of oriented attachment growth in vapor-solid process, which may be a result of high surface hydroxyl group density from extended H<sub>2</sub>O pulses.

Observation of the metastable phases and percolated films at high temperature is not accordant with the general understanding of ALD film growth and crystallization, which states that a crystalline film often starts with crystal nuclei followed by the self-limited layer-by-layer crystal growth.<sup>18,25</sup> In order to clearly illustrate such a unique nucleation process, atomic-scale elemental analysis was performed along the surface of a 10-cycle product, where the three typical transitional morphologies (film, flake, and particle) coexist (Figure 2a). From EELS collected over the three morphologies (Figure 2b–d), distinct Ti signals were identified on each of them (TiL3 at 458 eV and TiL2 at 463 eV).<sup>26</sup> Surface amorphous film (Figure 2b) and cloudy loosen flakes (Figure 2c) are the two first appearing nuclei forms. EELS spectra indicate that the density of Ti in such film/flake structures is much lower than that in the amorphous particles. The sparse amorphous nanoparticles are believed to be more stable nuclei form that were transformed from the flakes since a larger quantity of such particles was observed at longer growth cycles with the consumption of flakes (Figure 2d). At 25 cycles, crystalline phase (identified to be anatase) started to emerge inside amorphous particles. X-ray diffraction spectra (XRD) show that the anatase phase persisted

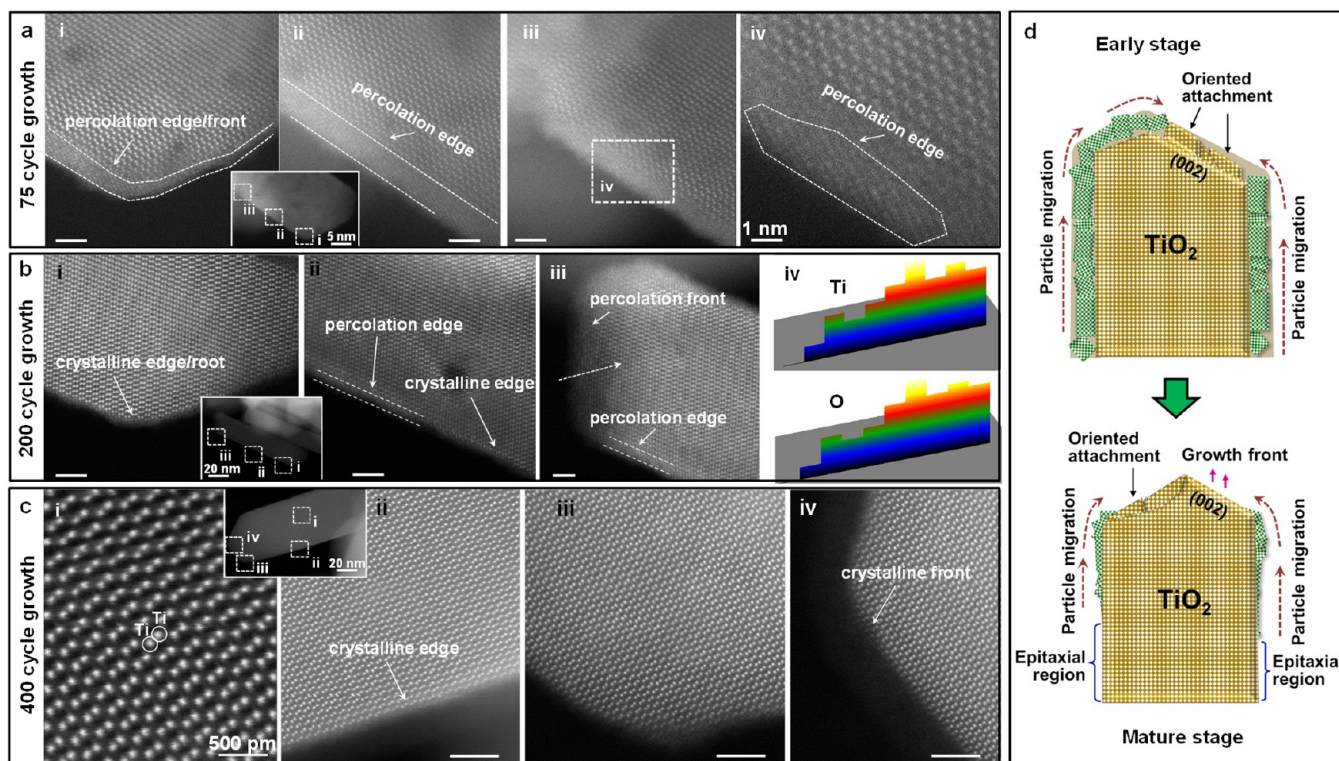


**Figure 3.** Vapor phase oriented attachment growth of TiO<sub>2</sub> NR by 600 °C ALD. (a) Atomic structure of NR grown at 75 cycles. Its tip (i), middle (ii), and root (iii) regions all have a 1–2 nm thick amorphous/crystalline percolated film, which is highlighted by the magnified root region (iv). (b) Atomic structure of NR grown at 200 cycles. (i) Well-defined (002) and (011) facets composing the NR root were found to be percolated film-free. (ii) A transient region with atomically flat (011) surface near the root of NR and percolated film-coated (011) surface near the tip region. (iii) The fuzzy NR tip with thicker percolated film. (iv) EELS line scan profiles show the growth front was much thinner in its outmost tip region while thicker close to its body. (c) Atomic structure of NR grown at 400 cycles. Its body (i), middle (ii), front (iii), and tip (iv) regions all exhibited high-quality crystal structure and are percolated film-free. No dislocation or stacking faults were spotted. The thick amorphous layer shown in (iv) is a result of carbon deposition during long-time imaging. (d) Schematics showing the oriented attachment process that is responsible for the anisotropic growth of a TiO<sub>2</sub> NR. Scale bars are 2 nm unless otherwise noted.

until the growth reached 900 cycles, where a slight amount of rutile structure started to appear (Supporting Information Figure S7). Therefore, the entire TiO<sub>2</sub> crystal evolution pathway at high-temperature (high-T) can be summarized as: amorphous film/flakes → amorphous particles → anatase → rutile.

Thermodynamic data from literature shows that  $-\Delta G_{f, \text{rutile}} > -\Delta G_{f, \text{anatase}} > -\Delta G_{f, \text{amorphous}}$ .<sup>27,28</sup> It has also been reported that the stability of such cloudy and loosen structures is generally much lower than a dense or crystalline phase in many crystal systems.<sup>29,30</sup> Thus, simple thermodynamic theory is not sufficient to explain the TiO<sub>2</sub> crystal evolution observed at 600 °C via ALD. The formation of transient metastable TiO<sub>2</sub> phases during the nucleation pathway in fact follows the empirical Ostwald–Lussac Law. This law states that an unstable system does not necessarily transform directly into the most stable phase but likely into one that most closely resembles itself.<sup>20,21</sup> In terms of energy, the phase transformation is always accompanied by the minimum energy loss. Such a non-equilibrium process therefore involves more kinetic concepts. To further prove the observed high-T TiO<sub>2</sub> crystal evolution is a case of Ostwald–Lussac Law, the nucleation process under 600 °C ALD was quantitatively modeled.

For any kinetically limited chemical process, the nucleation probability is proportional to the exponential of the barrier height divided by  $k_B T$ , where  $k_B$  is Boltzmann constant, and  $T$  is the nucleation temperature. The nucleation rate is given by<sup>31</sup>

$$J_n = A \exp\left(-\frac{\Delta g_n}{k_B T}\right) \quad (1)$$

where  $A$  is a constant factor. SI units are used for all terms units unless otherwise noted. The nucleation barrier can be substituted by surface free energy and supersaturation [ $\ln S$  (supersaturation) =  $AP$  (activity product)/ $K$  (equilibrium product)]. The supersaturation here deals with the chemically absorbed precursor molecules. In the case of high-temperature TiO<sub>2</sub> deposition, the active surface dangling bonds are considered movable and can be regenerated due to HCl side reactions.<sup>32</sup> Therefore, the chemically absorbed molecules could diffuse on the crystal or substrate surfaces, and form clusters and then nuclei for nanorod growth. The activity product is thus defined as that “activity of one gas-phase specie (water or TiCl<sub>4</sub>)” times “activity of available dangling bonds on substrates (Ti–Cl or O–H)”. Thus, the final form of nucleation rate can therefore be presented as (detailed derivation is given in S7),

$$J_n = A \exp\left(-B \frac{\gamma^3}{(\ln S)^2}\right) \quad (2)$$

where  $\gamma$  is the surface free energy of nucleus. Equation 2 suggests that the nucleation rate is strongly dependent on the second power of supersaturation and third power of surface free energy. Figure 2e shows the nucleation rates of amorphous

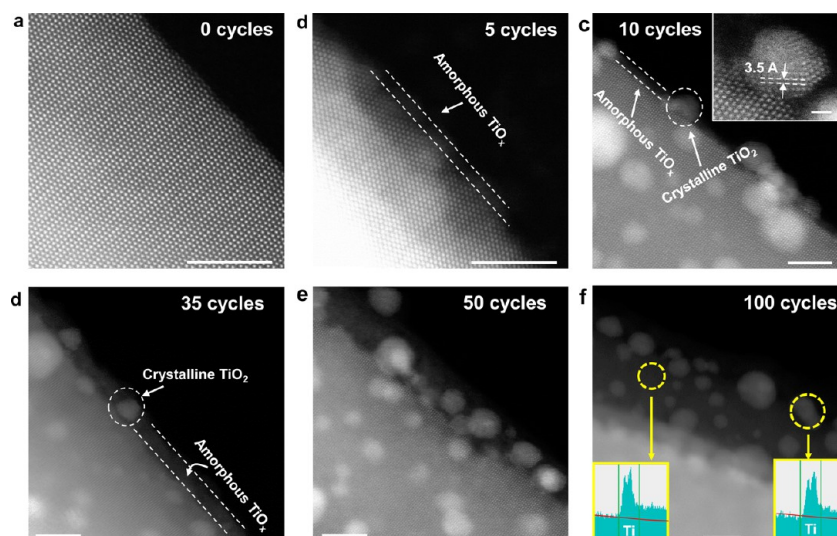


**Figure 4.** ALD growth of  $\text{TiO}_2$  film on ZnO NW at 300 °C. (a) A STEM image of a bare ZnO NW prior to ALD growth. (b) Five cycle growth: small amorphous  $\text{TiO}_2$  islands start to form on ZnO NW. (c) Ten cycle growth: crystalline  $\text{TiO}_2$  particles appeared with a thin but uniform and continuous amorphous  $\text{TiO}_2$  film covering the ZnO NW surface. Inset shows the crystallinity of a 2 nm  $\text{TiO}_2$  particle (scale bar is 1 nm). (d) Thirty-five cycle growth: both  $\text{TiO}_2$  crystalline particles and amorphous films grew larger and thicker. (e) Fifty cycle growth:  $\text{TiO}_2$  crystalline particles continued to grow larger and became buried by the thicker  $\text{TiO}_2$  film. (f) One Hundred cycle growth: amorphous  $\text{TiO}_2$  film reached  $\sim 10$  nm thick and various sized crystalline  $\text{TiO}_2$  particles were observed. The EELS analysis demonstrates that both amorphous and crystalline phases have similar amounts of Ti and Ti/O ratio. Scale bars are 5 nm unless otherwise noted.

film/flakes, amorphous particles, anatase, and rutile phases of  $\text{TiO}_2$  versus activity product of the precursors divided by the equilibrium product of amorphous particles. Solid lines are plotted based on above formulas and the dashed black line is deduced from our experimental observation. The color dash lines are applied to qualitatively illustrate the normalized equilibrium products of amorphous nanoparticles, anatase and rutile structures and the precursor activity. According to Figure 2e, though the supersaturation of anatase  $\text{TiO}_2$  is higher than amorphous nanoparticles at any randomly chosen considerable activity product ( $\ln S_{\text{anatase}} > \ln S_{\text{amorphous particle}}$ ), its nucleation rate is much lower than the amorphous nanoparticles. This perfectly agrees with our discovery from the 600 °C ALD results. The key factor yielding such a nucleation pathway is the drastic difference of surface free energies among different phases of  $\text{TiO}_2$ , which has more influence (3rd power) on the nucleation rates following eq 2: a smaller surface free energy yields a much higher nucleation rate. Atomic structure of disordered phase is closer to vapor precursors compared to well-crystallized ones, and thus possesses smaller surface free energy difference from vapor phase.<sup>33</sup> Literature reports revealed that the surface free energies of the three phases in Figure 2e follow the relation:  $\gamma_{\text{amorphous particles}} < \gamma_{\text{anatase}} < \gamma_{\text{rutile}}$ .<sup>27,34,35</sup> Therefore, the energy landscape of nucleation pathway from reaction precursors to final rutile phase is schematically illustrated in Figure 2f. Although Gibbs free energy change of anatase is larger than that of amorphous flakes/films, the much lower  $\gamma$  of amorphous flakes/films makes their nucleation energy barrier lower than that of direct formation of anatase phase, rendering a preferable nucleation route toward unstable amorphous phase at the beginning. This numerical analysis, together with the experimental observation, evidence that the  $\text{TiO}_2$  ALD growth at 600 °C follows the Ostwald–Lussac Law.

Regarding the  $\text{TiO}_2$  NR morphology evolution, the initial study shows that NRs started to form after  $\sim 50$  cycles of

growth. To further understand the anisotropic growth phenomenon that is responsible for NR formation, samples obtained from longer growth cycles were investigated. After 75 cycles of growth, HR HAADF STEM images revealed that the entire surface of single crystalline NR is covered with a  $\sim 2$  nm thick percolated film (a mixture of polycrystalline  $\text{TiO}_2$  with amorphous intercalation, Figure 3a). The atomic structure observed by the HR HAADF STEM is consistent with the anatase phase identified by XRD. The coexistence of amorphous and crystalline phases in the surface layer of  $\text{TiO}_2$  NR represents a similar case as that observed from Si NW surface in the nucleation stage. This is thus considered as the secondary nucleation on the surface of evolved  $\text{TiO}_2$  crystals, which still follows the Ostwald–Lussac Law. EELS line scans and mapping revealed a much lower Ti and O signal strength at the surface layer region compared to the NR body, indicating the crystalline layer is much less compact (Supporting Information Figure S8). From the 200-cycle sample, the base portion of the NR exhibited a clean and smooth surface; no percolated film or other defects were observed (Figure 3b-i). The percolated film started to appear at the middle region of the NR. It was a transient morphology with its thickness varying from a few angstroms (the bottom side) to  $\sim 1$  nm (the top side) (Figure 3b-ii). Fully evolved percolated film was only found at the top portion of NR (Figure 3b-iii). EELS line scan demonstrated that the outmost tip of NR contained much less Ti and O, indicating this was the region under development, or actively growing (Figure 3b-iv). After 400 cycles (Figure 3c), the NR's body (i), side surface (ii), and front (iii, iv) all exhibited high-quality crystallinity and no percolated film could be observed (the amorphous layer observed in Figure 3c-iv is due to carbon deposition in STEM chamber).

The  $\text{TiO}_2$  NR growth process can be observed more dynamically under TEM using electron beam illumination on a 75-cycle  $\text{TiO}_2$  NR embryo (Supporting Information Figure S9). The electron beam may induce local heating due to the poor

thermal conductivity of the sample, or knockout damage that largely increases the mobility of individual atoms. Either effect would facilitate the recrystallization of  $\text{TiO}_2$  and may recover the NR evolution process. TEM images along beam illumination show that the NR builds its body by sacrificing the surface percolated layers (evidenced by the shrinking of NR's diameter). This is because the surface crystallites are surrounded by amorphous films that are not epitaxially grown on the NR surface. When the mobility becomes high enough (e.g., under high temperature, 600 °C and hydroxyl group-rich environment), they could travel on the crystal surface and organize themselves to attach to appropriate NR surfaces following oriented attachment mechanism,<sup>23,36</sup> as schematically shown in Figure 3d. Annealing a  $\text{TiO}_2$  NR at 600 °C in the TEM chamber also provided supportive evidence to the oriented attachment-induced anisotropic NR growth (Supporting Information Figure S10). HRTEM images taken during the annealing process illustrate that at high temperature, the crystalline nanoparticle in the percolated film could align its crystal lattice with the NR lattice making the NR propagate along the (002) facet. Combining all above observations, we could suggest that the anisotropic growth is a result of shattering and migrating of percolated shells on manifold body and subsequent orientated attachment on high surface energy facet (the (002) facet of anatase  $\text{TiO}_2$ ).<sup>37–39</sup>

When the growth cycles approach 400, the density and surface area of NRs became much larger and the amount of precursor per unit area is much less than the early growth stages. Thus, once the value of  $\ln S$  is lower than both the equilibrium products of amorphous particles and even amorphous film/flake, nucleation of amorphous particles and film/flakes is ceased. According to Figure 2e, if the activity product is higher than the equilibrium product of anatase at this time, nucleation and growth of anatase would proceed on the NR surface. This is the scenario we have observed at this stage. Two hundred cycles result is more or less an intermediate phase between early cycles and high cycles, where precursors with a mean-free-path of a few hundred nanometers may not reach the root region of NRs and the nucleation and growth of anatase dominates in this region. At the top rim of NR, larger  $\ln S$  warrants the occurrence of nucleation and growth of amorphous phase.

The Ostwald–Lussac Law and orientated attachment observed in  $\text{TiO}_2$  NR growth was further explored in ALD anatase  $\text{TiO}_2$  films grown at 300 °C on ZnO NW sidewalls (Figure 4a). After five cycles of ALD growth, the NW's surface was covered with a discrete layer of amorphous  $\text{TiO}_x$  with the maximum thickness of 0.6 nm (Figure 4b). This corresponds to an averaged 0.06 nm per cycle, which is similar to low-temperature amorphous film growth rate.<sup>40</sup> After 10 cycles, a percolated film of crystalline  $\text{TiO}_2$  nanoparticles with amorphous  $\text{TiO}_x$  film matrix appeared (Figure 4c). The  $\text{TiO}_2$  nanoparticles did not exhibit any epitaxial relation with the ZnO lattice (inset of Figure 4c). The emergences of amorphous agglomerates and crystalline nanoparticles under 300 °C both occurred earlier than the 600 °C cases. Besides, diameter of the 10-cycle crystalline nanoparticles under 300 °C is  $\sim 2$  nm, twice larger than the 10-cycle crystallites grown at 600 °C. This indicates that the nucleation stage proceeds faster at 300 °C than 600 °C. The faster rate makes the transient amorphous particles phase unobservable at 300 °C. In order to understand the accelerated nucleation rate at lower temperature, the nucleation induction time is considered, which is given by,<sup>31</sup>

$$t_{\text{ind}} = kc^{1-p} \propto J_n^{-1} \quad (3)$$

where  $k$  is a constant,  $p$  is the number of molecules in a critical nucleus and  $c$  is the precursor concentration. According to eq 3,  $c$  at 300 °C should be much higher than at 600 °C. One likely reason is that molecules' desorption probability decreases exponentially with the temperature, while other parameters are less temperature dependent.<sup>31</sup> Therefore, at 300 °C the much lower desorption probability yields a significantly higher precursor molecule concentration on the surface, which renders a higher supersaturation ( $\ln S$ ) as an activity product of precursor molecules and corresponding active surface dangling bonds and thus results in a shorter nucleation induction time.

After 35 cycles of ALD, crystalline nanoparticles grew larger; meanwhile the amorphous islands coalesced and became a continuous amorphous film ( $\sim 2$  nm, Figure 4d). This result indicates that both phase transition (from amorphous to crystalline  $\text{TiO}_2$ ) and vapor deposition (propagation of amorphous layer) occurred simultaneously at 300 °C. As it proceeded to 50 cycles, the amorphous film reached  $\sim 5$  nm with most crystalline nanoparticles buried inside (Figure 4e). Figure 4f shows a 100-cycle ALD result, where a percolated nanoparticle-amorphous thin film ( $\sim 10$  nm in thickness) was obtained. Compositions of both nanoparticle and film are confirmed to be  $\text{TiO}_2$  by EELS. The 300 °C ALD process has two distinguishing differences compared to the 600 °C ALD: (1) the amorphous layer persists during the entire growth process; and (2) the small anatase nanoparticles do not agglomerate to form a NR embryo through the vapor-phase oriented attachment. The first difference is a direct outcome following the Ostwald–Lussac Law; while the second difference is governed by the oriented attachment principle. At 300 °C, coexistence of both amorphous and crystalline phases directly evidenced the operation of the Ostwald–Lussac Law. Whereas, the amorphous-to-crystalline ratio was much higher in the 300 °C products compared to the 600 °C products, indicating the phase transformation rate was much faster at 600 °C. This is consistent with the Ostwald–Lussac Law manifested in eq 1, in which the nucleation rate is strongly bounded to temperature. Oriented attachment requires that individual particles must have distinct facets, some of which have higher surface free energy in order to achieve anisotropic growth. Then self-organization proceeds by attaching neighboring crystalline nanoparticles onto high surface energy facets. At 300 °C, the diffusivity of amorphous  $\text{TiO}_x$  phase is much smaller than at 600 °C and therefore the formation of thermodynamically faceted particles become difficult, which disables the oriented attachment growth. In addition, mobility of crystalline particles has to be reasonable in order to enable orientation alignment and crystal attachment. Lower temperature (300 versus 600 °C) and the amorphous film coverage significantly restricted the mobility of the embedded nanoparticles. Last, lower temperature yielded a slower phase transition from amorphous film to crystalline particle and the accumulation of amorphous phase blocked the drifting of small particles for oriented attachment. This discovery suggests that the formation of a crystalline  $\text{TiO}_2$  ALD film may be a result of the combination of layer-by-layer surface chemical absorption and subsequent phase transformation.

This research revealed the role of the Ostwald–Lussac law in high-temperature  $\text{TiO}_2$  ALD growth processes. Atomic-resolution electron microscopy and elemental analysis manifest the evolution of  $\text{TiO}_2$  nanostructures during ALD follows a

generic and explicit path from amorphous layers to amorphous particles to metastable crystallites and ultimately to stable crystalline forms. The evolution can be terminated at any intermediate stage yielding thin films or nanostructures with mixed phases. At high temperature, the amorphous–crystalline mixture can enable a unique anisotropic crystal growth behavior forming TiO<sub>2</sub> nanorods via the principle of vapor-phase oriented attachment. This discovery provides a new understanding of morphology and property variation and phase nonuniformity in ALD thin films and nanostructures. It suggests that in order to achieve desired morphology, phase, and property of ALD products surface chemistry should not be the only consideration. Emphasis should also be placed on phase diagrams of target materials and local kinetics.

## ■ ASSOCIATED CONTENT

### Supporting Information

Supporting

Additional information and figures. This material is available free of charge via the Internet at <http://pubs.acs.org>.

## ■ AUTHOR INFORMATION

### Corresponding Author

\*E-mail: [xudong@engr.wisc.edu](mailto:xudong@engr.wisc.edu).

### Present Address

<sup>†</sup>(J.S.) School of Engineering and Applied Sciences, Harvard University.

### Notes

The authors declare no competing financial interest.

## ■ ACKNOWLEDGMENTS

The authors thank financial support from by U.S. Department of Energy, Office of Basic Energy Sciences under Award DE-SC0008711, and Air Force under Award FA9550-13-1-0168.

## ■ REFERENCES

- (1) George, S. M. Atomic Layer Deposition: An Overview. *Chem. Rev.* **2010**, *110*, 111–131.
- (2) Leskela, M.; Ritala, M. Atomic layer deposition (ALD): from precursors to thin film structures. *Thin Solid Films* **2002**, *409*, 138–146.
- (3) Niinisto, L.; Paivasaari, J.; Niinisto, J.; Putkonen, M.; Nieminen, M. Advanced electronic and optoelectronic materials by Atomic Layer Deposition: An overview with special emphasis on recent progress in processing of high-k dielectrics and other oxide materials. *Phys. Status Solidi A* **2004**, *201*, 1443–1452.
- (4) Wilk, G. D.; Wallace, R. M.; Anthony, J. M. High-kappa gate dielectrics: Current status and materials properties considerations. *J. Appl. Phys.* **2001**, *89*, 5243–5275.
- (5) Ando, T.; et al. Application of HfSiON to deep-trench capacitors of sub-45-nm-node embedded dynamic random-access memory. *Jpn. J. Appl. Phys., Part 1* **2006**, *45*, 3165–3169.
- (6) Huang, J. Y.; Wang, X. D.; Wang, Z. L. Controlled Replication of Butterfly Wings for Achieving Tunable Photonic Properties. *Nano Lett.* **2006**, *6*, 2325–2331.
- (7) Christensen, S. T.; et al. Supported Ru-Pt Bimetallic Nanoparticle Catalysts Prepared by Atomic Layer Deposition. *Nano Lett.* **2010**, *10*, 3047–3051.
- (8) Puurunen, R. L. Surface chemistry of atomic layer deposition: A case study for the trimethylaluminum/water process. *J. Appl. Phys.* **2005**, *97*, 121301.
- (9) Knez, M.; Niesch, K.; Niinisto, L. Synthesis and surface engineering of complex nanostructures by atomic layer deposition. *Adv. Mater.* **2007**, *19*, 3425–3438.

(10) Jur, J. S.; Parsons, G. N. Atomic Layer Deposition of Al<sub>2</sub>O<sub>3</sub> and ZnO at Atmospheric Pressure in a Flow Tube Reactor. *ACS Appl. Mater. Interfaces* **2011**, *3*, 299–308.

(11) Takahashi, N.; Nonobe, S.; Nakamura, T. Growth of HfO<sub>2</sub> films using an alternate reaction of HfCl<sub>4</sub> and O<sub>2</sub> under atmospheric pressure. *J. Solid State Chem.* **2004**, *177*, 3944–3948.

(12) Brennan, T. P.; et al. Atomic Layer Deposition of CdS Quantum Dots for Solid-State Quantum Dot Sensitized Solar Cells. *Adv. Energy Mater.* **2011**, *1*, 1169–1175.

(13) Dasgupta, N. P.; et al. Atomic Layer Deposition of Lead Sulfide Quantum Dots on Nanowire Surfaces. *Nano Lett.* **2011**, *11*, 934–940.

(14) Shi, J. A.; Sun, C. L.; Starr, M. B.; Wang, X. D. Growth of Titanium Dioxide Nanorods in 3D-Confined Spaces. *Nano Lett.* **2011**, *11*, 624–631.

(15) Shi, J.; Hara, Y.; Sun, C. L.; Anderson, M. A.; Wang, X. D. Three-Dimensional High-Density Hierarchical Nanowire Architecture for High-Performance Photoelectrochemical Electrodes. *Nano Lett.* **2011**, *11*, 3413–3419.

(16) Yang, R. B.; et al. The Transition between Conformal Atomic Layer Epitaxy and Nanowire Growth. *J. Am. Chem. Soc.* **2010**, *132*, 7592.

(17) Ritala, M.; Leskela, M. Atomic layer epitaxy - a valuable tool for nanotechnology? *Nanotechnology* **1999**, *10*, 19–24.

(18) Ritala, M.; Leskela, M.; Nykanen, E.; Soininen, P.; Niinisto, L. Growth of Titanium-Dioxide Thin-Films by Atomic Layer Epitaxy. *Thin Solid Films* **1993**, *225*, 288–295.

(19) Liu, Y. Q.; Xu, M.; Heo, J.; Ye, P. D. D.; Gordon, R. G. Heteroepitaxy of single-crystal LaLuO<sub>3</sub> on GaAs(111)A by atomic layer deposition. *Appl. Phys. Lett.* **2010**, *97*, 162910.

(20) Ferguson, J. Biological Mineralization and Demineralization - Nancollas, G. *Miner. Mag.* **1983**, *47*, 421–421.

(21) Pellegrino, E. D. Biological Mineralization and Demineralization - Report of the Dahlem Workshop on Biological Mineralization and Demineralization, Berlin, October 18–23, 1981 - Nancollas, G. *Q. Rev. Biol.* **1983**, *58*, 611–611.

(22) Ostwald, W. Studien über die Bildung und Umwandlung fester Körper. *Z. Phys. Chem* **1897**, *22*, 289–330.

(23) Penn, R. L.; Banfield, J. F. Imperfect oriented attachment: Dislocation generation in defect-free nanocrystals. *Science* **1998**, *281*, 969–971.

(24) Penn, R. L.; Banfield, J. F. Oriented attachment and growth, twinning, polytypism, and formation of metastable phases: Insights from nanocrystalline TiO<sub>2</sub>. *Am. Mineral.* **1998**, *83*, 1077–1082.

(25) Miiikkulainen, V.; Leskela, M.; Ritala, M.; Puurunen, R. L. Crystallinity of inorganic films grown by atomic layer deposition: Overview and general trends. *J. Appl. Phys.* **2013**, *113*, 021301.

(26) Brydson, R.; et al. Electron Energy-Loss Spectroscopy (EELS) and the Electronic-Structure of Titanium-Dioxide. *Solid State Commun.* **1987**, *64*, 609–612.

(27) Ranade, M. R.; et al. Energetics of nanocrystalline TiO<sub>2</sub>. *Proc. Natl. Acad. Sci. U.S.A.* **2002**, *99*, 6476–6481.

(28) Barin, I.; Knacke, O. *Thermochemical Properties of Inorganic Substances*; Springer-Verlag: New York, 1973.

(29) Yau, S. T.; Petsev, D. N.; Thomas, B. R.; Vekilov, P. G. Molecular-level thermodynamic and kinetic parameters for the self-assembly of apoferritin molecules into crystals. *J. Mol. Biol.* **2000**, *303*, 667–678.

(30) Yau, S. T.; Vekilov, P. G. Quasi-planar nucleus structure in apoferritin crystallization. *Nature* **2000**, *406*, 494–497.

(31) De Yoreo, J. J.; Vekilov, P. G. Principles of crystal nucleation and growth. *Biomaterialization* **2003**, *54*, 57–93.

(32) Wang, X.; Shi, J. Evolution of titanium dioxide one-dimensional nanostructures from surface-reaction-limited pulsed chemical vapor deposition. *J. Mater. Res.* **2013**, *28*, 270–279.

(33) Yau, S. T.; Vekilov, P. G. Direct Observation of Nucleus Structure and Nucleation Pathways in Apoferritin Crystallization. *J. Am. Chem. Soc.* **2001**, *123*, 1080–1089.

- (34) Zhang, H. Z.; Banfield, J. F. Kinetics of Crystallization and Crystal Growth of Nanocrystalline Anatase in Nanometer-Sized Amorphous Titania. *Chem. Mater.* **2002**, *14*, 4145–4154.
- (35) Zhang, H. Z.; Banfield, J. F. Understanding Polymorphic Phase Transformation Behavior during Growth of Nanocrystalline Aggregates: Insights from TiO<sub>2</sub>. *J. Phys. Chem. B* **2000**, *104*, 3481–3487.
- (36) Lovley, D. R. Geomicrobiology: Interactions between microbes and minerals. *Science* **1998**, *280*, 54–55.
- (37) Oskam, G.; Nellore, A.; Penn, R. L.; Searson, P. C. The Growth Kinetics of TiO<sub>2</sub> Nanoparticles from Titanium(IV) Alkoxide at High Water/Titanium Ratio. *J. Phys. Chem. B* **2003**, *107*, 1734–1738.
- (38) Barnard, A. S.; Zapol, P.; Curtiss, L. A. Modeling the morphology and phase stability of TiO<sub>2</sub> nanocrystals in water. *J. Chem. Theory Comput.* **2005**, *1*, 107–116.
- (39) Diebold, U.; Ruzycski, N.; Herman, G. S.; Selloni, A. One step towards bridging the materials gap: surface studies of TiO<sub>2</sub> anatase. *Catal. Today* **2003**, *85*, 93–100.
- (40) Wilson, C. A.; Grubbs, R. K.; George, S. M. Nucleation and Growth during Al<sub>2</sub>O<sub>3</sub> Atomic Layer Deposition on Polymers. *Chem. Mater.* **2005**, *17*, 5625–5634.

# Supporting Online Materials

## Electron Microscopy Observation of TiO<sub>2</sub> Nanocrystal Evolution in High-Temperature Atomic Layer Deposition

Jian Shi,<sup>1,†</sup> Zhaodong Li,<sup>1</sup> Alexander Kvit,<sup>1,2</sup> Sergiy Krylyuk,<sup>3</sup> Albert V. Davydov,<sup>3</sup> Xudong Wang<sup>1,\*</sup>

1. Department of Materials Science and Engineering, University of Wisconsin-Madison

2. Materials Science Center, University of Wisconsin-Madison

3. National Institute of Standards and Technology

† Current address: School of Engineering and Applied Sciences, Harvard University

\* Email: [xudong@engr.wisc.edu](mailto:xudong@engr.wisc.edu)

## S1: Experimental Details of Materials Growth

### (1) Setup and Conditions of Atomic Layer Deposition (ALD)

TiO<sub>2</sub> thin films and nanorods (NRs) were grown in a home-made ALD facility. Separated exposures of gaseous TiCl<sub>4</sub> and H<sub>2</sub>O vapors were controlled by solenoid valves and adjusted by fine tuning the precursor tank temperature. In details, substrates [Si nanowires (NWs) or ZnO NWs] were placed at the center of the ALD chamber (stainless steel tube with a diameter of 2 inch) and 10 cm downstream away from the precursor injection nozzle. During the growth, a constant flow of 40 sccm N<sub>2</sub> was applied into the chamber as the carrier gas, which provided a background pressure of 2.7 Torr. The chamber temperature was maintained at 300 °C or 600 °C. In a typical TiO<sub>2</sub> NRs (at 600 °C) process, TiCl<sub>4</sub> and H<sub>2</sub>O vapor precursors were pulsed into the chamber for 1 s each and separated by purging N<sub>2</sub> for 60 s. Thus, one growth cycle includes 1 s of H<sub>2</sub>O pulsing + 60 s of N<sub>2</sub> purging + 1 s of TiCl<sub>4</sub> pulsing + 60 s of N<sub>2</sub> purging. For TiO<sub>2</sub> polycrystalline thin film (at 300 °C) growth, the TiCl<sub>4</sub> and H<sub>2</sub>O precursor pulses were both 0.5 s and separated by 60 s N<sub>2</sub> purging. After growth, the chamber cooled down to room temperature naturally under N<sub>2</sub> flow. To prepare the different stages of nanostructure/film, growth was interrupted at the ALD growth cycles of 2, 5, 10, 20, 25, 35, 50, 75, 100, 200, 300 and 400. Figure S1 presents the low-magnification scanning transmission electron microscopy (STEM) images of TiO<sub>2</sub> morphologies on Si nanowires (NWs) grown in different ALD cycles at 600 °C. All nanostructures observed and compared were prepared under the same ALD growth conditions.

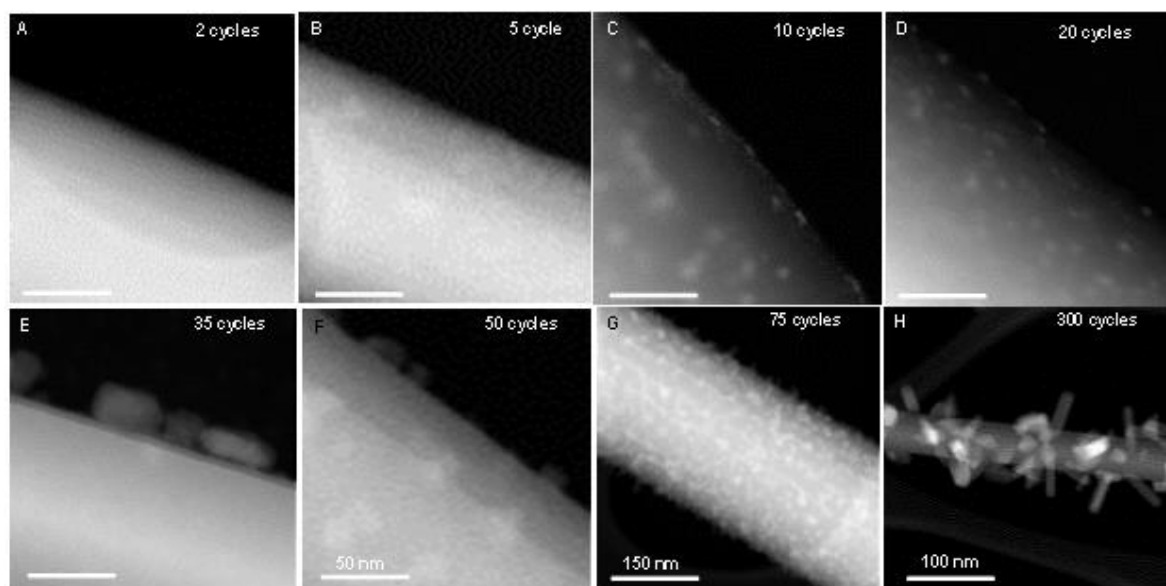


**Fig. S1. Low magnification of STEM images at different ALD stages (scale bars are 20 nm unless otherwise noted).**

## (2) Growth of ZnO NWs by Chemical Vapor Deposition (CVD)

A horizontal tube furnace system was used to perform the vapor deposition of ZnO NW. A small quartz tube 25 cm in length and 1.6 cm in inner diameter was used to support the precursor and substrate and increase the vapor concentration. In a typical process, ZnO powder (0.3 g) and graphite powder (0.3 g) were mixed and ground together and placed in a quartz boat positioned 5 cm from one end in the quartz tube. A 500-nm-thick GaN epilayer covered sapphire substrate was used for ZnO nanostructure deposition. The substrates were 8 cm away from the source boat. This small quartz tube was then placed into a large alumina tube in the tube furnace with the source boat aligned at the center of the tube furnace and the substrates located on the downstream side of the carrier gas. The carrier gas used throughout the experiments was 1% oxygen balanced by high purity argon. First, the furnace was quickly increased to 925 °C at a ramp rate of 50 °C/min. When the temperature reached 400 °C, the carrier gas was introduced into the deposition system with a flow rate of 50 sccm and the system pressure was brought to 20 Torr. Then the furnace temperature was held at 925 °C for 30 min for ZnO NW deposition. At this temperature, according to the temperature profile of this furnace, the local substrate temperature was 900 °C. Finally, the furnace was turned off and the system was allowed to cool down naturally without changing the system pressure and carrier gas flow.

## (3) Growth of Si NW by CVD

Gold-catalyzed Si NWs were grown in a home-built hot-wall CVD system at 900 °C and 80 kPa (600 Torr) reactor pressure using 30 sccm (standard cm<sup>3</sup>/min) of silicon tetrachloride and 200 sccm of hydrogen diluted with nitrogen to a total flow rate of 1000 sccm. SiCl<sub>4</sub> vapor was delivered by nitrogen carrier gas through a bubbler with liquid SiCl<sub>4</sub> held at 15 °C and 104 kPa (780 Torr). Au nanoparticles (100 nm in diameter) dispersed on poly-L-lysine-functionalized Si(111) substrate were utilized to facilitate the vapor-liquid-solid (VLS) growth mechanism of the NWs.

## (4) Characterization

All HR-HAADF-STEM, TEM, HRTEM images, and EELS characterization were conducted in a C<sub>s</sub>-corrected FEI Titan microscope operated at 200 kV. HAADF STEM images were collected with a 24.5 mrad probe semiangle, and 24.5 pA probe current. *in-situ* TEM heating holder from Hummingbird was used to dynamically observe the crystal structural evolution of TiO<sub>2</sub> NRs heated to be 600 °C.

## S2: Crystal Structure of Small Crystallites

One distinguishable feature of HRTEM (high resolution transmission electron microscopy) image from HR-STEM (high resolution scanning transmission electron microscopy) is that it provides phase contrast to differentiate the amorphous phase from crystalline region. As a supplemental instrumentation, we apply HRTEM to confirm the crystal structure of small crystallites grown at 35 cycles of 600 °C ALD. HRTEM image (Fig. S2) indicates that there is always a thin layer of amorphous TiO<sub>2</sub> wrapping the crystallites, which is often a few angstroms thick. Each polycrystalline assemblage is composed of a few individual small crystallites.

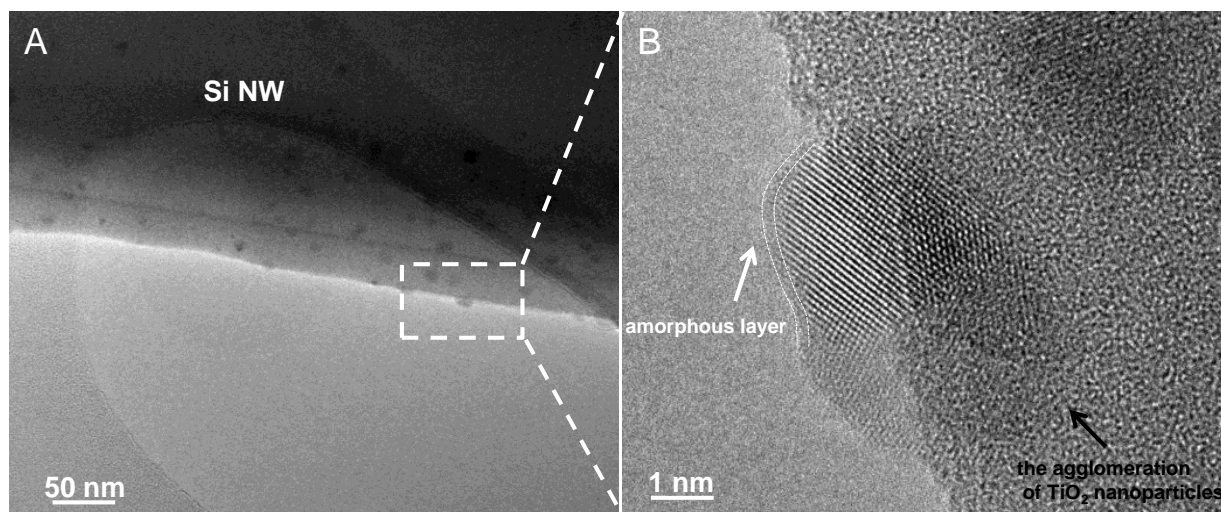


**Figure S2. TEM images of 35 cycles ALD growth at 600 °C. (A)** Size distribution of 35 cycles ALD growth results on Si NWs. **(B)** An amorphous sub-nanometer-thick TiO<sub>2</sub> layer covering the surface of the crystallites assemblage.

## S3: Conformal NRs Growth by 600 °C ALD

CVD Si NWs arrays were used as growth substrates to investigate the conformity and size distribution of 600 °C ALD TiO<sub>2</sub> NRs. Length of these Si NWs is usually above 10 μm and their diameters range from a few tens of nanometers to several hundred nanometers. In a very typical growth recipe of 1 s of H<sub>2</sub>O pulsing + 60 s of N<sub>2</sub> purging + 1 s of TiCl<sub>4</sub> pulsing + 60 s of N<sub>2</sub> purging, conformal NRs coating was achieved across the whole Si NW axial direction. Figure S3 shows that the density and size of TiO<sub>2</sub> NRs acquired from the base region of Si NWs is more or less similar to the top rim of NWs, demonstrating a powerful technique/growth mode for hierarchical NW-NR structure fabrication.

The merit of this NR growth approach is the ability to deposit high density NR arrays inside highly confined submicrometer spaces. In our previous work, we demonstrated the deposition of TiO<sub>2</sub> NRs around dense Si NWs forest, as shown in Fig. S4 (obtained from our previous publication *Nano Letters*, 11, 3413-3419, 2011). This structure offers tremendous surface area per unit substrate area as well as excellent charge transport property. Therefore, they are a very promising 3D nanostructure for developing high-performance photovoltaic and photoelectrochemical electrodes.

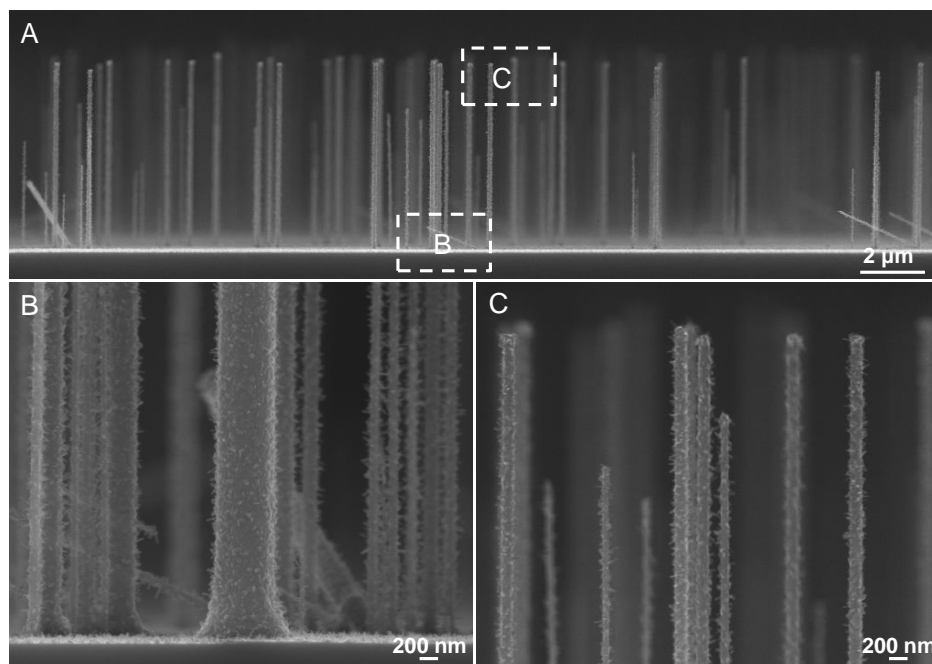


**Figure S3. SEM images of 400 cycles ALD growth of TiO<sub>2</sub> NRs on single crystalline Si NWs arrays. (A) Low magnification SEM image of Si NWs arrays. Growth of TiO<sub>2</sub> NRs on the base (B) and tip rim (C) of Si NWs.**

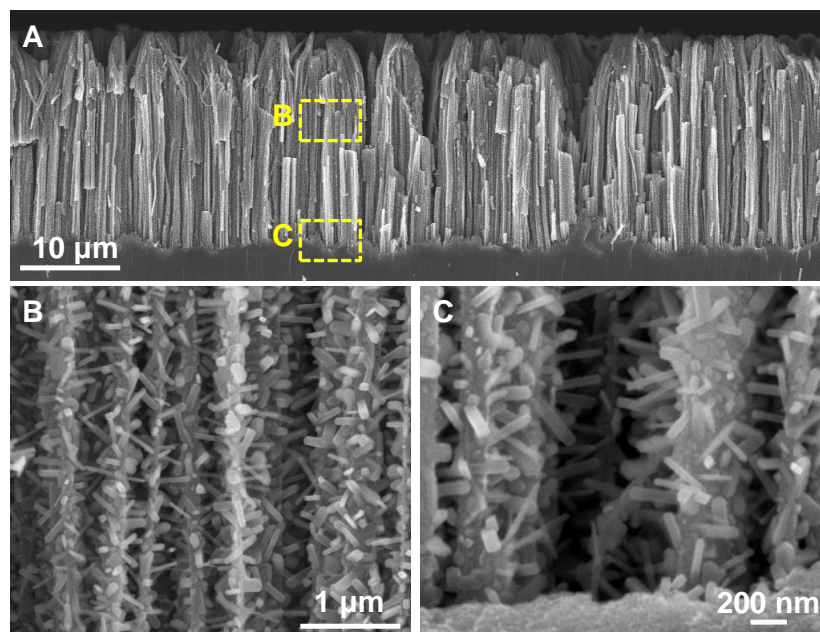


**Figure S4. SEM images of TiO<sub>2</sub> NRs grown inside high-density Si NW forest.** (A) Cross-section of vertical Si NW arrays covered with TiO<sub>2</sub> NRs. The Si NWs are ~25 μm long and the top ~5 μm region was bundled together. (B, C) The middle and bottom portions of Si NWs showing dense and uniform coverage of TiO<sub>2</sub> NRs along the entire NW length. (from reference *Nano Letters*, 11, 3413-3419, 2011).

#### **S4: Phase Transformation and Self-organization of Crystallites**

In order to further confirm the amorphous phase of the small particles we observed on the surface of Si NWs by HR-STEM, HRTEM was utilized for phase identification. As shown in Fig. S5A, these small (~ 1nm in width) amorphous particles have a relatively sparse distribution on the Si NW surfaces. Because HRTEM is not Z-contrast-based, often only half of these amorphous particles' body would show up from the Si NW. Their amorphous structure can be clearly evidenced from the HR image (Fig. S5B). As the growth proceeds to 25 cycles, individual crystalline TiO<sub>2</sub> particle is identified as shown in Fig. S5C, which is believed to be transformed from the amorphous particles formed in the earlier stages. An amorphous layer can also be spotted on the surface of the single crystalline particles. At 25 cycles, polycrystalline assemblage is also observed, which consists of a few small particles aligning along the same orientation (Fig. S5D), suggesting the occurrence of self-organization of TiO<sub>2</sub> crystallites by following oriented attachment growth mechanism.

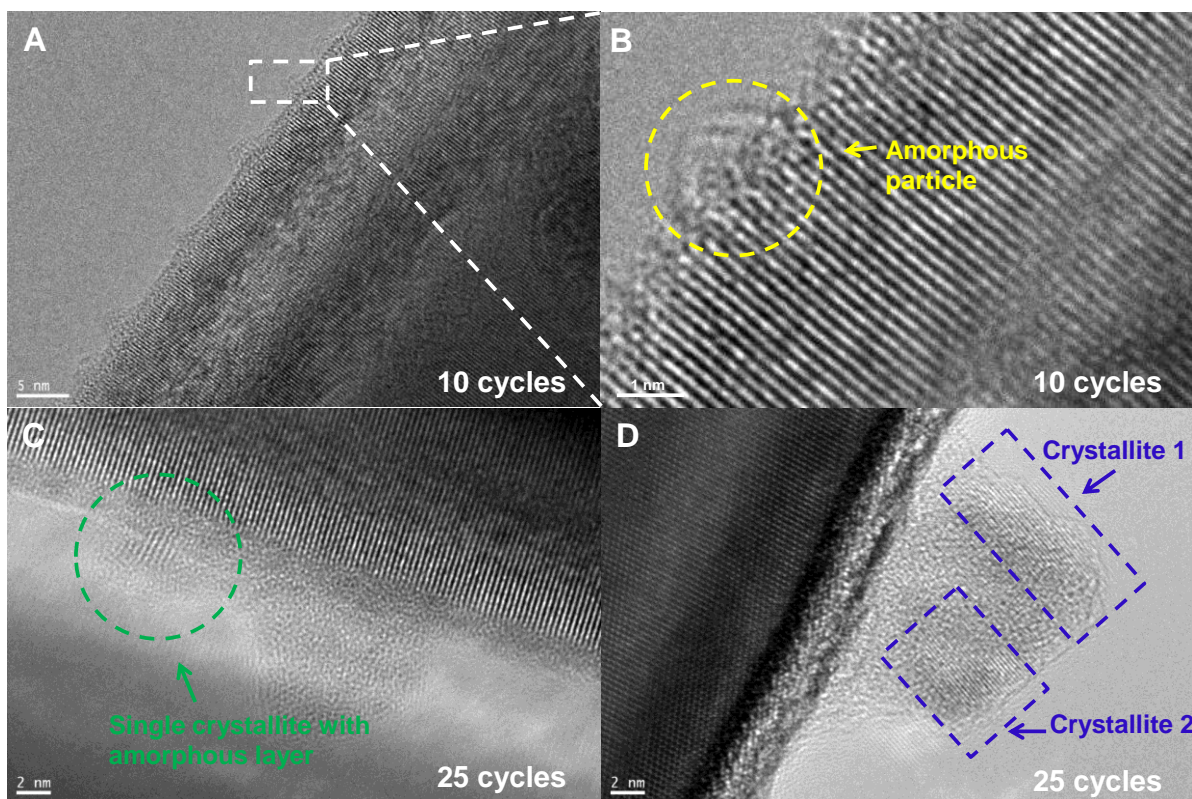


**Figure S5. Phase transformation and self-organization of crystallites.** (A, B) High resolution TEM images of amorphous TiO<sub>2</sub> nanoparticles growing on single crystalline Si NWs after 10 cycles ALD growth at 600 °C. (C) Presence of TiO<sub>2</sub> crystallites coated by a thin layer of amorphous film after 25 cycles growth of ALD at 600 °C. (D) Self-organization of small crystallites along certain crystallographic orientation suggesting the concurrence of oriented attachment growth mechanism.

### S5: Supportive Evidence of Vapor Phase Oriented Attachment

To further evidence the evolution of TiO<sub>2</sub> NRs embryos follows the vapor phase oriented attachment mode, we attempt to simulate this process in TEM chamber and simultaneously monitor the morphology development (Fig. S6). We firstly grew a 25 cycles of ALD amorphous TiO<sub>2</sub> layer at 120 °C with extend water pulse (2 s) on silicon nitride membrane TEM grid, then immediately loaded the sample inside TEM chamber for electron beam radiation. Right after 1 minute TEM beam radiation, several small TiO<sub>2</sub> crystallites formed a chain by aligning them along one certain orientation. This chain became larger when the radiation time reached 2 minutes and finally a NR embryo started to present after 5 minutes. This observation is supportive evidence to the vapor-phase oriented attachment growth mechanism.

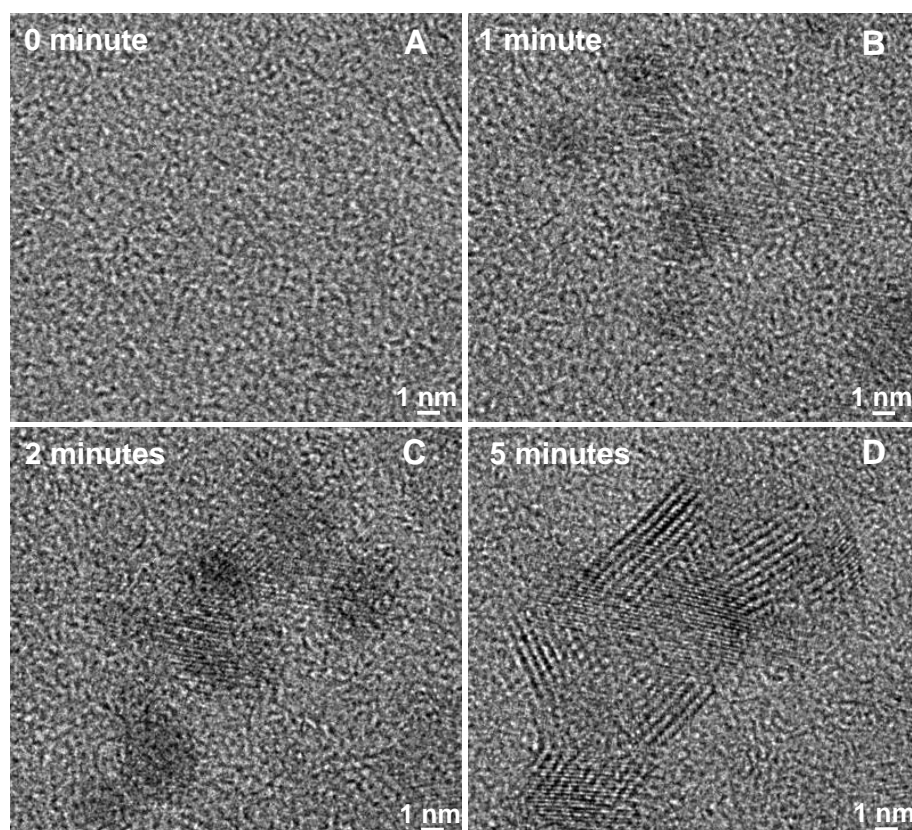


**Figure S6. Oriented attachment growth mechanism simulated by TiO<sub>2</sub> nanoparticles grown on silicon nitride membrane TEM grid.** (A) As-coated amorphous TiO<sub>2</sub> film on SiN membrane prior to electron beam illumination. (B) Formation of a nanochain by self-organization of small TiO<sub>2</sub> crystallites along one crystallographic orientation after 1 minute electron beam radiation. (C) Propagation of the nanochain formed at stage (B) by attaching more small crystallites after 2 minutes electron beam radiation. (D) The continuous expanding and elongation of the nanochain by more oriented attachment growth after 5 minutes illumination. The superlattice formed in (D) is believed to be consequence of the imperfect crystallite alignment/organization.

### S6: The Emergence of Rutile Structure

According to Ostwald-Lussac Law, eventually we should expect the presence of rutile structure after a very long growth period. To search for such evidence, we have prepared the ALD TiO<sub>2</sub> structures grown at 660 cycles, 900 cycles and 1200 cycles at 600 °C. X-ray diffraction (XRD) was conducted to reveal the phase evolution from anatase to ultimate rutile structure. It was found that at 660 cycles, the TiO<sub>2</sub> is still pure anatase (Fig. S7). When the growth proceeds to 900 cycles, the rutile phase starts to appear though still as the minority. As growth goes to 1200

cycles, the relative ratio of rutile to anatase increases illustrated by the intensities of their corresponding XRD peaks. Such finding fits in the derivation from Ostwald-Lussac Law.

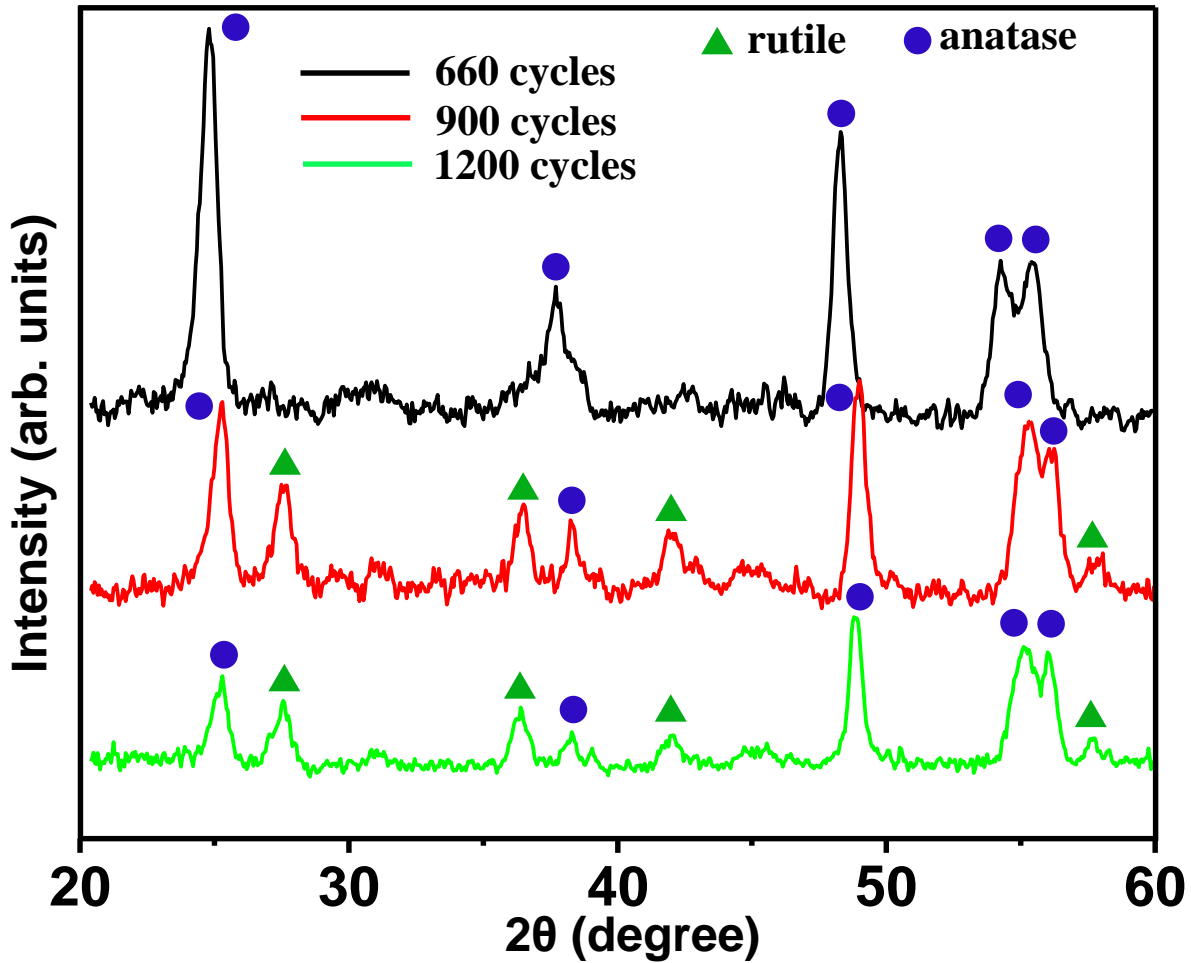


**Figure S7.** X-ray diffraction spectra of TiO<sub>2</sub> NRs grown at 660, 900 and 1200 cycles. At 660 cycles, the NRs were still pure anatase phase while at 990 cycles, the rutile phase started to appear and its relative amount to the anatase phase further increased at 1200 cycles.

### S7: Derivation of Nucleation Rates

The general nucleation rate is given by,

$$J_n = A \exp\left(-\frac{\Delta g_n}{k_B T}\right),$$

where  $k_B$  is Boltzmann constant,  $T$  is the nucleation temperature,  $A$  is a constant and  $\Delta g_n$  is the nucleation barrier.

For a heterogeneous nucleation, nucleation barrier is,

$$\Delta g_n = \frac{(16/3)\pi\gamma^3v^2}{(k_B T \ln S)^2},$$

where  $v$  is the molecular volume,  $\ln S$  is the supersaturation, and  $\gamma$  is the surface free energy of nucleus, which is given by,

$$\gamma = \gamma_{gc}\{1 - (\gamma_{gs} - \gamma_{sc})/2\gamma_{gc}\},$$

According to the 10- and 20-cycle growth results, most amorphous nanoparticles exhibit very large contact angle on the NW surface. Thus to first order approximation,  $\gamma$  is simplified to be  $\gamma_{gc}$  in our subsequent calculations. The nucleation rate therefore is obtained as,

$$J_n = A \exp\left(-B \frac{\gamma^3}{(\ln S)^2}\right),$$

where B is a constant.

### **S8: Secondary Nucleation on Single Crystalline TiO<sub>2</sub> Surface**

The emergence of single crystalline TiO<sub>2</sub> NRs inevitably provides a new growth surface for ALD TiO<sub>2</sub> film/crystal nucleation. The TiO<sub>2</sub> amorphous-crystalline percolated shell on the TiO<sub>2</sub> NR body is therefore believed to be the result of the expected secondary nucleation deposition, which also follows the Ostwald-Lussac Law. High resolution electron energy loss spectroscopy (EELS) map and line scan revealed that such percolated shell was much less compact than the NR body (Fig. S8).

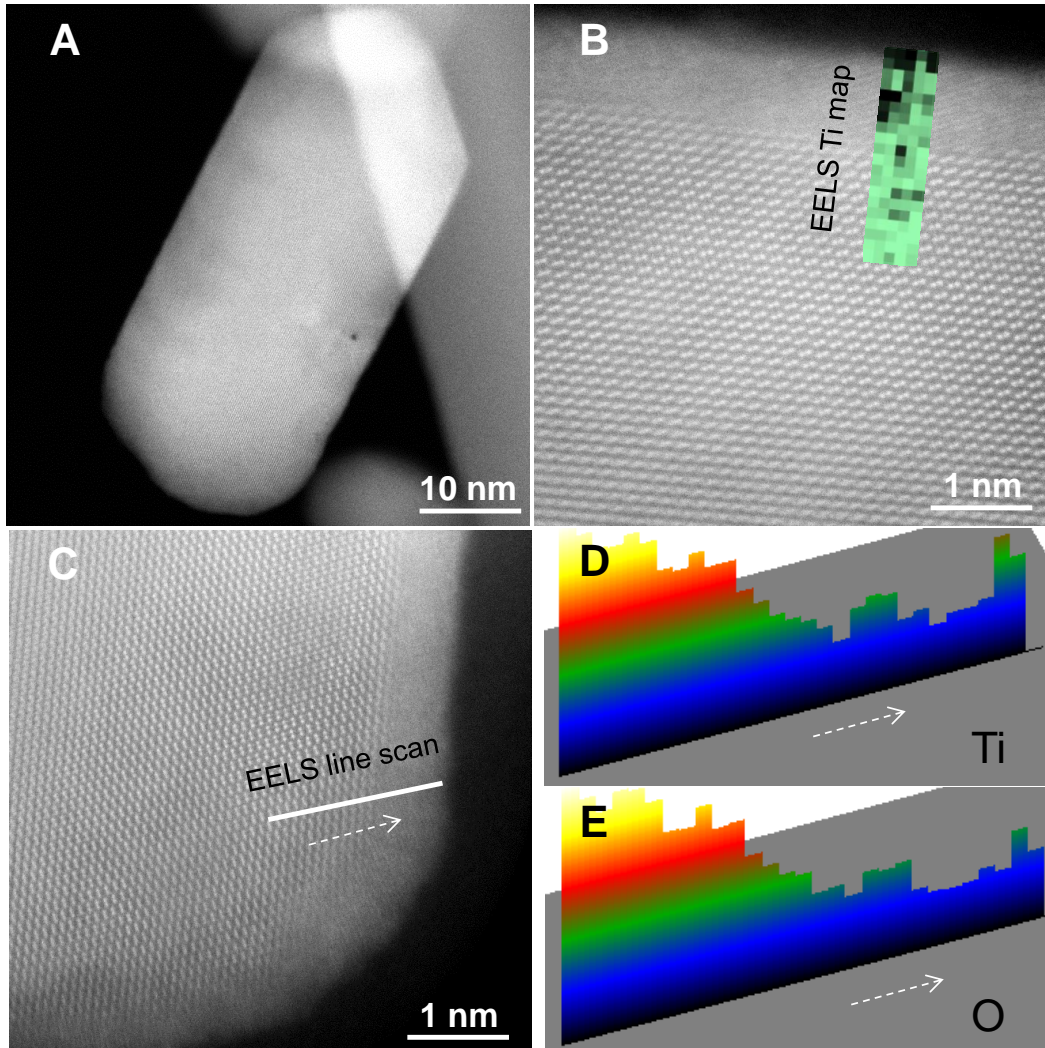


**Figure S8. EELS characterization of 100 cycles TiO<sub>2</sub> NRs grown at 600 °C ALD.** (A) Low magnification STEM image showing the overall morphology of the NR anchoring on the Si NW. (B) Atomistic EELS Ti map across the percolated film-single crystalline region of NR with brighter color illustrating more Ti and darker color for less Ti. (C) HR STEM image of the TiO<sub>2</sub> NR covered with an amorphous layer, where EELS line scan is indicated. (D, E) are the Ti and O EELS signal profiles, respectively, along the NR edge. They demonstrate that the percolated surface film is much less compacted than the NR body.

### S9: TEM Beam Illumination-Induced NR Growth

To investigate the NR growth mode during intermediate ALD cycles (75 cycles) and explore the evolution of the percolated TiO<sub>2</sub> shells formed in the secondary nucleation process, we grew a TiO<sub>2</sub> NR embryo at 75 cycles *via* 600 °C ALD and then immediately loaded it into TEM chamber for characterization. Here, TEM electron beam was used as to radiate the TiO<sub>2</sub> crystal

and activate the recrystallization. Meanwhile, HRTEM images were captured every 1 minute after beam radiation. The electron beam may induce local heating due to the poor thermal conductivity of the sample, or knock-out damage that largely increases the mobility of individual atoms. Either effect would facilitate the recrystallization of TiO<sub>2</sub> and may recover the NR evolution process. EELS maps (not shown here) demonstrate that the NR investigated usually consist of two major regions: thick and thin (Fig. S9A). Along with the time of beam radiation, the thick region propagates while the thin part shrinks (Fig. S9B and C). The width of NR is found to be narrowed down after 2 minutes beam heating suggesting the sacrificing of percolated TiO<sub>2</sub> shells for NR growth.

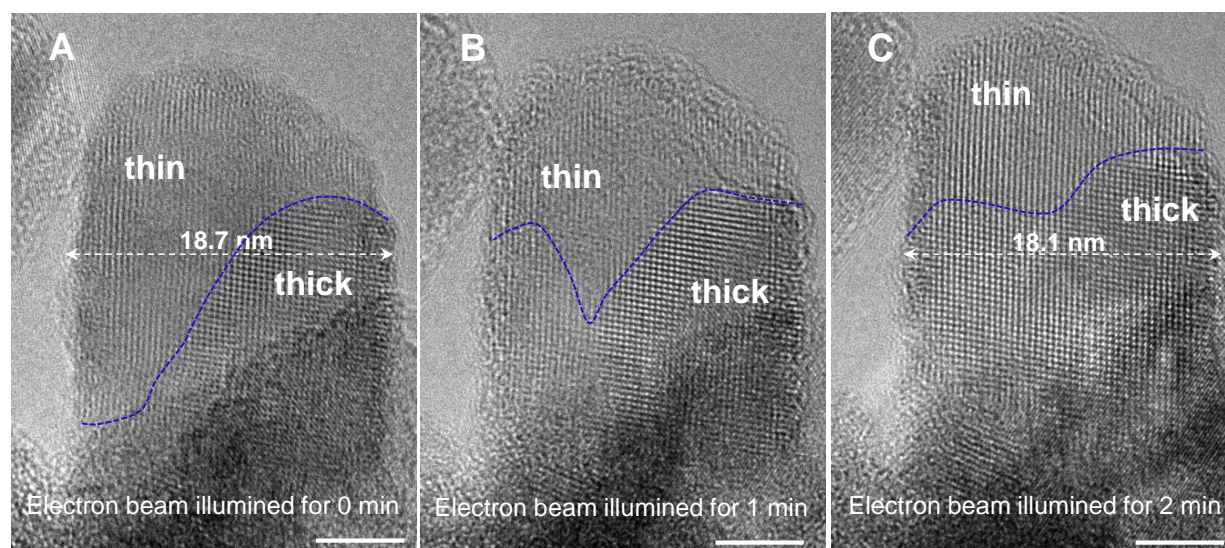


**Figure S9. Electron beam-induced 75 cycles NR growth during TEM chamber.** (A) A HRTEM image of TiO<sub>2</sub> NR prior to electron beam illumination. The NR consists of three distinct regions: thick region, thin region and percolated film sidewalls. The thickness of the NR at the indexed location at this stage is 18.7 nm. Blue dash line is used to outline the boundary between the thick and thin regions. (B) With 1 minute TEM beam illumination, the thick region advances while the thin region shrinks. (C) After 2 minutes beam illumination, the thick region keeps propagating and thin region becomes less. The diameter of the NR at the specific location at this stage is found to be smaller (18.1 nm) indicating the consumption of percolated regions. All scar bars are 5 nm.

### S10: *In-situ* Thermal Heating-Induced Crystal Growth

As discussed in the main text and previous reference (*Nano Letters*, 11, 3413-3419, 2011), the TiO<sub>2</sub> NR (002) facet is the active growth front. By *in situ* heating of a TiO<sub>2</sub> NR with its (002) facet coated by the percolated TiO<sub>2</sub> shell, we attempted to directly observe the growth process on the active facet (Fig. S10). To enable such experiment, we firstly grew TiO<sub>2</sub> NRs via 400 cycles

ALD then coated the NRs with a 5-cycle ALD TiO<sub>2</sub> film at 300 °C. Afterwards, we loaded the sample into TEM chamber anchored on a TEM heating holder. The temperature of the NR was ramped to 600 °C in 1 minute and kept for 5 minutes. Right before and after annealing, HRTEM images were captured. It shows that small crystallites on the (002) surface prior to annealing realigned themselves to incorporate on the NR (002) facet after annealing while other facets of NR did not exhibit sensible change. Such observation confirms that (002) is the active growth plane, which is a consequence of its high surface free energy and consistent with the oriented attachment growth mechanism.

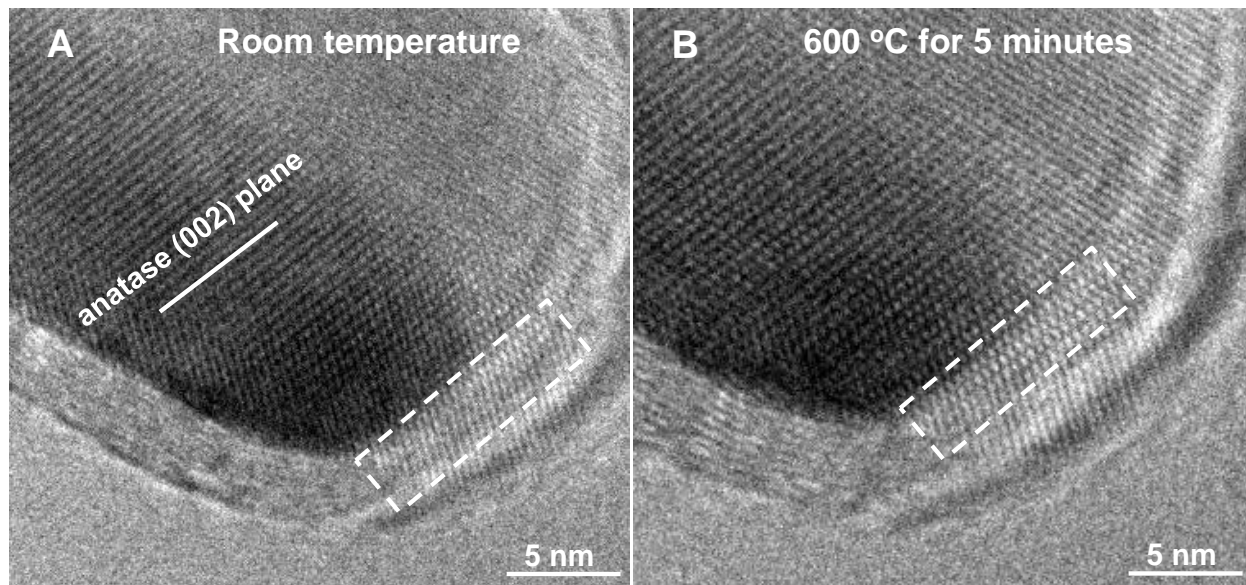


**Figure S10. *in situ* heating of 400 cycles TiO<sub>2</sub> NR in a TEM heating holder.** (A) HRTEM image of NR tip at room temperature prior to thermal heating. Dash rectangle indicates the existence of a percolated layer on the NR tip. (B) After ramping the temperature to 600 °C in 1 minute and then holding at 600 °C for 5 minutes, the percolated film transformed to a part of single crystalline anatase phase, suggesting the self-organization of small crystallites onto NR body for oriented attachment growth during thermal heating. The thick amorphous layer is due to the carbon deposition during TEM imaging and thermal heating.